The microstructure of scale formed by oxynitriding of Ti and exhibiting significant apatite-forming ability

Masami Hashimoto, Satoshi Kitaoka

Japan Fine Ceramics Center

2-4-1 Mutsuno, Atsuta-ku, Nagoya, 456-8587 Japan

Shunsuke Muto and Kazuyoshi Tatsumi

EcoTopia Science Institute, Nagoya University

Furo-cho, Chikusa-ku, Nagoya, 464-8603 Japan

Yoshihiro Obata

Graduate School of Engineering, Nagoya University

Furo-cho, Chikusa-ku, Nagoya, 464-8603 Japan

*) To whom correspondence should be addressed: Masami Hashimoto

Japan Fine Ceramics Center

2-4-1 Mutsuno, Atsuta-ku, Nagoya, 456-8587 Japan

Tel. +81-52-871-3500, Fax +81-52-871-3599

E-mail: masami@jfcc.or.jp

Satoshi Kitaoka

E-mail: kitaoka@jfcc.or.jp

Shunsuke Muto

E-mail: s-mutoh@nucl.nagoya-u.ac.jp

Kazuyoshi Tatsumi

E-mail: k-tatsumi@nucl.nagoya-u.ac.jp

Yoshihiro Obata

E-mail: obata.yoshihiro@a.mbox.nagoya-u.ac.jp

ABSTRACT

A scale formed by heat treatment of Ti in a nitrogen atmosphere containing oxygen at an extremely low partial pressure exhibited an exceptional degree of HAp formation in a simulated body fluid. STEM and EELS indicated that the subsurface of this scale was composed of nitrogen doped rutile-type TiO_2. The N-K edge energy-loss near edge structure spectrum for this layer in conjunction with the theoretical spectra for possible compounds obtained using the augmented plane wave plus local orbital band method suggested that oxygen sites were replaced by two nitrogens, resulting in an effective charge of +2. The enhanced HAp forming ability of this scale is likely related to the positively charged surface induced by the presence of N. Conversely, the subsurface scale formed by heat treatment in air, in which N is not found, leads to much slower HAp coverage, believed to be related to the lack of surface charge.

Keywords:

Ti / scanning transmission electron microscopy / electron energy-loss spectroscopy

1. Introduction

Titanium (Ti) is widely used in artificial joints because of its high fracture toughness and good biocompatibility. However, Ti does not bond to living bone and thus its fixation relative to the surrounding bone is not stable over the long term. Several methods have been developed to impart bone-bonding ability to Ti [1-5]. In general, bioactive materials in the body bond to living bone through a hydroxyapatite (Hap) layer. HAp formation is a complex process that involves controlled nucleation and growth from an aqueous solution. Since negative and positive charged surfaces can induce HAp formation, the generation of HAp initiated via calcium or phosphate ion adsorption upon complexation with negatively or positively charged surfaces, respectively, may be the dominant process. Once HAp nuclei are formed, they grow by the uptake of calcium and phosphate ions from surrounding body fluids.

Wang et al. was able to improve the hydroxyapatite (HAp)-forming ability of Ti through the formation of a surface scale produced by the oxidation of Ti [6-8]. Recently, we have shown that the heat treatment of Ti in a nitrogen atmosphere with a precisely regulated oxygen partial pressure (P_{O2}) of 10^{-14} Pa at 973 K for 1 h (treatment A) forms a scale containing rutile-type TiO_2 with strongly enhanced HAp formation potential compared to that of the scale obtained in air with a P_{O2} of 10^4 Pa (treatment B) [9].

The HAp formation kinetics on this scale, described using the Avrami-Erofeev equation, exhibit a significant dependence on the P_{O2} in the nitrogen atmosphere. Following treatment A, the Avrami index for the scale was n=2 when immersed in a simulated body fluid (SBF) with ion concentrations nearly equal to those in human blood plasma and serving as the medium for HAp nucleation at 309.5 K. This value implies the instantaneous nucleation of HAp, which proceeds to completely cover the scale surface in a short time span. In contrast, in the case of treatment B, the Avrami index for the scale was n=3, indicating that the HAp nuclei were

sparsely distributed and formed at a constant rate, taking a long time to cover the scale surface [10].

To examine the relationship between the type of scale and its HAp forming ability, the scale surfaces have been analyzed using X-ray photoelectron spectroscopy (XPS) and zeta potential measurements. The surface charges on scales formed using treatment A were found to be highly positive, with a zeta potential of approximately 20 mV, whereas the scales formed with treatment B had zeta potentials close to zero. The XPS-N1s spectra of the surfaces of scales formed with treatment A suggested the presence of rutile-type TiO_2 containing nitrogen (N). However, the state of the N and the origin of the positive zeta potential were not determined.

Applying a statistical signal processing technique to spectrum imaging (SI) datasets obtained by scanning transmission electron microscopy (STEM) combined with electron energy loss spectroscopy (EELS), particularly core state excitation spectral energy-loss near edge structure (ELNES) analyses, can resolve the overlapping spectral components, thereby visualizing the spatial distribution of each different chemical state as a relative concentration map on the nano level [11-13].

In the present study, the presence and microstructure of N in the scales formed by treatments A and B were precisely determined by applying this statistical signal processing technique to STEM-EELS data, comparing the experimental and theoretical N-K edge ELNES spectra of the TiO_2 layer. The cause of the significant positive charge on the outermost surface of the treatment A scale and the associated acceleration of HAp formation are discussed based on the resulting information.

2. Materials and methods

2.1. Scale formation

A commercially-obtained sample of pure Ti (>99.9%, Nilaco Co., Tokyo, Japan) with dimensions of 10 × 10 × 1 mm was employed. The surface of the Ti was polished with a mirror plane and subsequently cleaned with acetone, 2-propanol and distilled water in an ultrasonic bath for 30 min intervals. The Ti was then placed in a furnace, the atmosphere of which was replaced with P_{O2}-controlled nitrogen (N_2) gas (P_{O2} = 10^{-14} Pa) using a solid-state electrochemical oxygen pump system. The gas flow rate in this apparatus was 3×10^{-4} m^3/min. The Ti was heated from ambient to 973 K at a rate of 5 K/min and then held at this temperature for 1 h, maintaining a P_{O2} value of 10^{-14} Pa in the nitrogen atmosphere, representing treatment A. Finally, the Ti was cooled to room temperature at a rate of 5 K/min. Treatment in a commercially-obtained simulated air mixture was also performed for comparison purposes, representing treatment B.

2.2. SIMS analysis

The N and O depth profiles in the scales formed by treatments A and B were determined using a PHI ADEPT1010 secondary ion mass spectrometer (SIMS), employing a Cs^+ primary ion beam at a 5 kV impact voltage for sputtering.

2.3. STEM-EELS spectral imaging and MCR analysis

In preparation for STEM-EELS analyses, cross-sectional specimens were prepared by argon milling (GATAN model 691) of samples to a depth of approximately 20 μm below the surface of the scales formed by treatments A and B. STEM-EELS spectral imaging data were acquired at room temperature using a Jeol JEM 2100 STEM system for the high energy region (including O-K, N-K and Ti-$L_{2,3}$ edges). This instrument was equipped with a Gatan Enfina 1000

spectrometer with a probe size of 2 nm, and an acquisition time of 0.5 s and a scan step of 5 nm were applied [14, 15]. The energy dispersion was set to 0.3 eV channel^{-1} with an energy loss range from 370 to 570 eV. Spectral drift correction, pre-edge background subtraction and deconvolution to remove plural scattering were all performed.

Spectral image datacubes were obtained by scanning the nanosized electron probe over wide areas of the sample of interest and analyzing the resulting data using the statistical multivariate curve resolution (MCR) method to extract the embedded spectral components and map their two-dimensional spatial distributions [11-13].

2.4. Theoretical N-K ELNES calculations

Theoretical ELNES spectra for possible nitrogen-related defects in rutile-type TiO_2 (denoted as $(X)_i(V)$: X (defect species) = N, N_2, NO, NO_2, *i* (occupying site) = O (oxygen site) or I (interstitial site) and V (effective charge of the defect) = -2 to +3, varying with the possible electron occupancies of the induced band-gap states) were calculated by the pseudopotential plane wave band method within the generalized gradient approximation (GGA [16]; CASTEP code [17]). This allowed comparison of the relative peak intensities and positions of the experimental and theoretical spectra. A 2 × 2 × 3 supercell consisting of a primitive cell containing 72 atoms of the rutile structure per supercell with a core hole introduced at the excited atom was used. Prior to the spectral calculations, the structural parameters were optimized using the same software package. The atom positions were freely relaxed while applying the constraints of the given symmetry of the supercell within the fixed supercell size until the residual force was reduced to less than 0.05 eVÅ^{-1}. The final ELNES spectrum was broadened using three functions; a Gaussian function with a FWHM (full width at half maximum) of Γ = 1.0 eV, a Lorentzian function with Γ = 0.18 eV, and a Lorentzian function with $\Gamma = 0.1E$, where *E* is an energy value above the threshold. These three functions correspond to instrumental

broadening, core-hole lifetime broadening and excited electron lifetime broadening, respectively. As an accuracy check, it was confirmed that the relative peak energy positions calculated using the CASTEP and WIEN2k (via the all electron full potential method) codes deviated by less than 1 eV [18].

3. Results and discussion

3.1. Ti, O and N distributions in scales

Figure 1 presents a cross-sectional TEM image and the N and O SIMS depth profiles for the scale formed by treatment A. Here, the SIMS intensities are normalized to that for Ti. It is evident that the thickness of the scale formed on the Ti is approximately 200 nm, and that it has a double layered structure, primarily consisting of O–rich columnar crystals at the surface side and fine N-rich crystals at the substrate side. The thin-film X-ray diffraction (XRD) pattern for the scale surface in a previous study [10] and the TEM electron diffraction pattern of the cross-section of the scale in the present study identify these O-rich and N-rich layers as rutile-type TiO_2 and TiN, respectively. Using the FactSage free-energy minimization computer code together with the FactPS and FToxid databases, the equilibrium partial pressure of O_2 at the interface between the TiO_{2-x} and TiN was calculated thermodynamically to be 10^{-23} Pa at 973 K. Consequently, the TiN layer is believed to have formed at the interface by the inward diffusion of N into the scale and the simultaneous reduction of the oxygen chemical potential (μ_O).

Figure 2 shows a cross-sectional TEM image and N and O SIMS depth profiles for the scale formed by treatment B. This scale was about 1-2 μm thick and also had a layered structure composed of rutile-type TiO_2 at the surface side and TiN closer to the substrate. However, the N/Ti ratio of the interface near the substrate in the TiO_2 formed by treatment B was obviously less than that in the treatment A scale.

3.2. Spatial distributions of product phases in the scale

The cross section of the scale formed by treatment A (Figure 3(a)) was examined by STEM-EELS spectral imaging, and the Ti, O and N elemental distributions throughout the framed area in Figure 3(a) were determined, as shown in Figures 3(b)-(d). In these images, pores are evident approximately 30 nm below the surface in the middle of the upper TiO_2 layer. This suggests that the fluxes associated with the outward diffusion of Ti ions and the inward diffusion of oxygen ions through the TiO_2 layer were drastically increased at this position. This divergence of the ion fluxes is likely related to void formation, and similar behavior has been reported in the case of NiO and CoO scales formed on the corresponding metals [19-20].

Considering the elemental distributions, the most likely phases are the metallic titanium substrate, followed by TiN and TiO_2 moving from bottom to top, although the top oxide layer also contains a small amount of nitrogen. This is consistent with the N K, Ti $L_{2,3}$ and O K ELNES profiles presented in Figure 4(b), extracted from the depth regions indicated by the solid broken lines in Figure 4(a). It is also noteworthy that the nitrogen concentration of the top oxide layer is not uniform, but rather decreases when approaching the surface.

In order to visualize the distributions of phases rather than elements, an MCR technique based on non-negative matrix factorization [11-13] was applied to the same three sets of EEL spectral data shown in Figure 4, the results of which are provided in Figure 5. Judging from the random statistical noise in the residual components, three significant phases were identified, and their spectral profiles are shown in Figure 6. As predicted from the elemental maps in Figure 4(b), phases I, II and III can be identified, consisting of the metallic titanium, nitrogen-doped TiO_2 and slightly oxidized TiN.

The chemical state of nitrogen in the top layer of the treatment A scale can be considered by focusing on the N K ELNES data for phase II, presented in Figure 6(a). Because of its low concentration (~1 at%), the spectral profile exhibits some noise features although it can be

characterized by the distinct sharp peak around 400 eV. The chemical states associated with the spectral features can discussed based on first principles theoretical simulations using several conceivable structural models.

Figure 7 shows the experimental and theoretical N-K ELNES spectra of the N-doped TiO_2 formed by treatment A. The theoretical energy loss axis was corrected so that the onsets of the experimental and theoretical N-K spectra of TiN (not shown here) were coincident, and the theoretical $(N_{2O})(+2)$ spectrum was shifted by the same relative energy difference. The signal at 400 eV in the experimental spectrum is consistent with that in the theoretical $N_{2O}(+2)$ spectrum, in which N_2 was substituted at the oxygen site in TiO_2 and had an effective charge of +2. Thus, the positive charge of $N_{2O}(+2)$ is thought to be responsible for the significant positive surface charge of the scale formed by treatment A. It is this charge that effectively promotes the formation of HAp nuclei through the initial attraction of negatively charged phosphate ions, followed by positively charged calcium ions. Although the peak shapes and positions in the theoretical spectra for N-related defects such as $(NO)_O$ and $(NO)_O(-1)$ were almost equivalent to those in the experimental spectra, the N-related defect formation energies differed from that of $N_{2O}(+2)$ [21]. It has been reported that N will substitute at the oxygen site (N_O) in TiO_2, with a resulting effective charge of -1 in the N-doped TiO_2, which subsequently exhibits high photocatalytic activity [21-31]. The N configuration in this N-doped photocatalyst was obviously different from that in the N-doped TiO_2 with significant HAp forming ability generated in the present study. Thus, treatment A can effectively promote HAp formation, but not does not produce photocatalytic activity.

The results of the two-component MCR analysis of the subsurface scale formed by treatment B are summarized in Figure 8, in which two significant components are identified. The spectral profiles for these phases are shown in Figure 9. Both phases I and II can be identified as rutile-type TiO_2, containing no N atoms. It should also be noted that the oxygen content in the

subsurface scale formed by treatment B was apparently higher than that in the treatment A scale. The subsurface scale without N is considered to represent a zero charge surface, predicted to be much less active with regard to promoting the growth of HAp on the scale.

4. Conclusions

The microstructures of scales formed on Ti substrates by heat treatment either in a N_2 atmosphere containing extremely low oxygen partial pressure (P_{O2}) or in air were analyzed by SIMS, STEM and EELS. The scale obtained under a low P_{O2} in N_2 exhibited high HAp forming ability and was composed primarily of a rutile-type N-doped TiO_2 layer at the surface side and a TiN layer at the substrate side. Comparing the experimental and theoretical N-K ELNES spectra of the N-doped TiO_2, N was found to have substituted at oxygen sites in the TiO_2, providing an effective charge of +2. The high HAp forming ability of the scale is likely attributable to the positively charged surface induced by the presence of N in the TiO_2 layer. In contrast, the subsurface scale formed by heat treatment in air, that did not contain N in the subsurface, was considered to have a neutral surface and was much less active with regard to the formation of HAp.

Acknowledgments

This work was supported in part by a Grant-in-Aid for Scientific Research on Innovative Areas “Nano Informatics” (nos. 25106008 and 25106004) and by a Kibankenkyu A grant (no. 26249096) from the Japan Society for the Promotion of Science (JSPS).

References

[1] H. M. Kim, F. Miyaji, T. Kokubo, and T. Nakamura: Preparation of bioactive Ti and its alloy via simple chemical surface treatment. *J. Biomed. Mater. Res.* **32**, 409 (1996).

[2] T. Kokubo, D. K. Pattanayak, S. Yamaguchi, H. Takadama, T. Matsushita, T. Kawai, M. Takemoto, S. Fujibayashi, and T. Nakamura: Positively charged bioactive Ti metal prepared by simple chemical and heat treatments. *J. R. Soc. Interface* **7**, 503 (2010).

[3] T. Kawai, T. Kizuki, H. Takadama, T. Matsushita, H. Unuma, T. Nakamura, and T. Kokubo: Apatite formation on surface titanate layer with different Na content on Ti metal. *J. Ceram. Soc. Japan* **118**, 19 (2011).

[4] M. Kawashita, N. Matsui, T. Miyazaki, and H. Kanetaka: Effect of autoclave and hot water treatments on surface structure and in vitro apatite-forming ability of NaOH- and heat-treated bioactive titanium metal. *Materials Transactions* **54**, 811 (2013).

[5] T. Shozui, K. Tsuru, S. Hayakawa, and A. Osaka: Enhancement of in vitro apatite-forming ability of thermally oxidized titanium surfaces by ultraviolet irradiation. *J. Ceram. Soc. Jpn.* **116**, 530 (2008).

[6] X. X. Wang, W. Yan, S. Hayakawa, K. Tsuru, and A. Osaka: Apatite deposition on thermally and anodically oxidized titanium surfaces in a simulated body fluid. *Biomaterials* **24**, 4631 (2003).

[7] K. Uetsuki, H. Kaneda, Y. Shirosaki, S. Hayakawa, and A. Osaka: Effects of UV-irradiation on in vitro apatite-forming ability of TiO_2 layers. *Mat. Sci. Eng. B* **173**, 213 (2010).

[8] Y. Xie, X. Liu, A. Huang, C. Ding, and P. K. Chu: Improvement of surface bioactivity on titanium by water and hydrogen plasma immersion ion implantation. *Biomaterials*, **26**, 6129 (2005).

[9] M. Hashimoto, K. Kashiwagi, and S. Kitaoka: A nitrogen doped TiO_2 layer on Ti metal for the enhanced formation of apatite. *J. Mater. Sci. Mater. Med.* **22**, 2013 (2011).

[10] M. Hashimoto, K. Hayashi, and S. Kitaoka: Enhanced apatite formation on Ti metal heated in P_{O2}-controlled nitrogen atmosphere. *Mat. Sci. Eng. C* **33**, 4155 (2013).

[11] S. Muto, T. Yoshida and K. Tatsumi: Diagnostic nano-analysis of materials properties by multivariate curve resolution applied to spectrum images by S/TEM-EELS. *Mater. Trans.* **50**, 964 (2009).

[12] S. Muto, Y. Sasano, K. Tatsumi, T. Sasaki, K. Horibuchi, Y. Takeuchi and Y. Ukyo: Capacity-fading mechanisms of $LiNiO_2$-based lithium-ion batteries II. Diagnostic analysis by electron microscopy and spectroscopy. *J. Electrochem. Soc*. **156**, A371 (2009).

[13] S. Muto, K. Tatsumi, T. Sasaki, H. Kondo, T. Ohsuna, K. Horibuchi and Y. Takeuchi: Mapping of heterogeneous chemical states of lithium in a $LiNiO_2$-based active material by electron energy-loss spectroscopy. Electrochem. Solid State Lett. **13**, A115 (2010).

[14] Y. Kojima, S. Muto, K. Tatsumi, H. Kondo, H. Oka, K. Horibuchi, and Y. Ukyo: Degradation analysis of a Ni-based layered positive-electrode active material cycled at elevated temperatures studied by scanning transmission electron microscopy and electron energy-loss spectroscopy. *J. Power Sources* **196**, 7721 (2011).

[15] S. Muto, K. Tatsumi, Y. Kojima, H. Oka, H. Kondo, K. Horibuchi, and Y. Ukyo: Effect of Mg-doping on the degradation of $LiNiO_2$-based cathode materials by combined spectroscopic methods. *J. Power Sources* **205**, 449 (2012).

[16] J.P. Perdew, K. Burke and M. Ernzerhof: Generalized gradient approximation made simple. *Phys. Rev. Lett.***77** 3865 (1996).

[17] S. J. Clark, M. D. Segall, C. J. Pickard, P. J. Hasnip, M. J. Probert, K. Refson, M. C. Payne: First principles methods using CASTEP. *Zeitschrift fuer Kristallographie* **220**, 567 (2005).

[18] P. Blaha, K. Schwarz, G. K. H. Madsen, D. Kvasnicka, J. Luitz: Wien2k, an augmented plane wave + local orbitals program for calculating crystal properties (*Karlheinz Schwarz, Techn. Universität Wien, Austria*), 2001, ISBN: 3-9501031-1-2.

[19] K. Akiba, M. Ueda, K. Kawamura, and T. Maruyama: Quantitative prediction of voids formation in a growing nickel oxide scale at 1373K. *Mater. Trans.*, **48**, 2753 (2007).

[20] K. Akiba, M. Ueda, K. Kawamura, and T. Maruyama: Quantitative prediction of voids formation in a growing cobaltous oxide scale at 1373K. *Mater. Trans.*, **48**, 2997 (2007).

[21] J. B. Varley, A. Janotti, and C. G. Van de Walle: Mechanism of visible-light photocatalysis in nitrogen-doped TiO_2. *Adv. Mater.* **23**, 2343 (2011).

[22] Y. Kihn, C. Mirguet, and L. Calmels: EELS studies of Ti-bearing materials and ab initio calculations. *J. Electro. Spectro. Related Phenom.* **143**, 117 (2005).

[23] R. Asahi, T. Morikawa, T. Ohwaki, K. Aoki, and Y. Taga: Visible-light photocatalysis in nitrogen-doped titanium oxides. *Science* **293**, 269 (2001).

[24] R. Asahi, and T. Morikawa: Nitrogen complex species and its chemical nature in TiO_2 for visible-light sensitized photocatalysis. *Chem. Phys.* **339**, 57 (2007).

[25] T. Yoshida, S. Muto, and J. Wakabayashi: Depth-resolved EELS and chemical state mapping of N^+-implanted TiO_2 photocatalyst. *Mat. Trans.*, **48**, 2580 (2007).

[26] T. Yoshida, and S. Muto: Chemical state analyses of nitrogen implanted titanium dioxide photocatalyst by means of XAFS, TEM and EELS. *AMTC Letters* **1**, 118 (2008).

[27] I. Takahashi, D. J. Payne, R. G. Palgrave, and R. G. Egdell: High resolution X-ray photoemission study of nitrogen doped TiO_2 rutile single crystals. *Chem. Phys. Lett*. **454**, 314 (2008).

[28] S. Lee, I. S. Cho, D. K. Lee, D. W. Kim, T. H. Noh, C. H. Kwak, S. Park, K. S. Hong, J. K. Lee, and H. S. Jung: Influence of nitrogen chemical states on photocatalytic activities of nitrogen-doped TiO_2 nanoparticles under visible light. *J. Photochem. and photobio. A: Chemistry*, **213**, 129 (2010).

[29] M. Xing, J. Zhang, and F. Chen: New approaches to prepare nitrogen-doped TiO_2 photocatalysts and study on their photocatalytic activities in visible light. *Applied Catalysis B:*

Environ. **89**, 563 (2009).

[30] Y. Wang, C. Feng, M. Zhang, J. Yang, and Z. Zhang: Enhanced visible light photocatalytic activity of N-doped TiO_2 in relation to single-electron-trapped oxygen vacancy and doped-nitrogen. *Applied Catalysis B: Environ.* **100**, 84 (2010).

[31] Y. Chen, X. Cao, B. Lin, and B. Gao: Origin of the visible-light photoactivity of NH_3-treated TiO_2: effect of nitrogen doping and oxygen vacancies. *Appl. Surf. Sci*. **264**, 845 (2013).

Figure captions

FIG. 1. Cross-sectional TEM image (left) and N and O SIMS depth profiles (right) through the scale formed by treatment A. The SIMS intensities have been normalized to the Ti intensity.

FIG. 2. Cross-sectional TEM image (left) and N and O SIMS depth profiles (right) through the scale formed by treatment B. The SIMS intensities have been normalized to the Ti intensity.

FIG. 3. Depth-resolved Ti, N and O distributions in the scale formed by treatment A, obtained by scanning the framed area in (a) (5 nm / pixel).

FIG. 4. STEM image (left) and depth-resolved Ti-$L_{2,3}$ O-K and N-K edge ELNES spectra (right) of a cross-section of the scale formed by treatment A.

FIG. 5. Three component MCR analysis of the scale formed by treatment A: (a) STEM image of the scale, and spatial distribution maps from the framed area of (b) phase I, (c) phase II, (d) phase III and (e) the residual phase.

FIG. 6. Ti-$L_{2,3}$ O-K and N-K edge ELNES spectra of the extracted spectral components of phases I, II and III in the scale formed by treatment A. Each spectrum is shifted vertically for better show.

FIG. 7. Experimental and theoretical N-K ELNES spectra in the vicinity of the surface of the scale formed by treatment A.

FIG. 8. Two-component MCR analysis of the scale formed by treatment B: (a) STEM image of the scale, and spatial distribution maps from the framed area of (b) phase I, (c) phase II and (d) the residual phase.

FIG. 9. Ti-$L_{2,3}$ O-K and N-K edge ELNES spectra of the extracted spectral components of phases I and II in the subsurface scale formed by treatment B. Each spectrum is shifted vertically for better show.

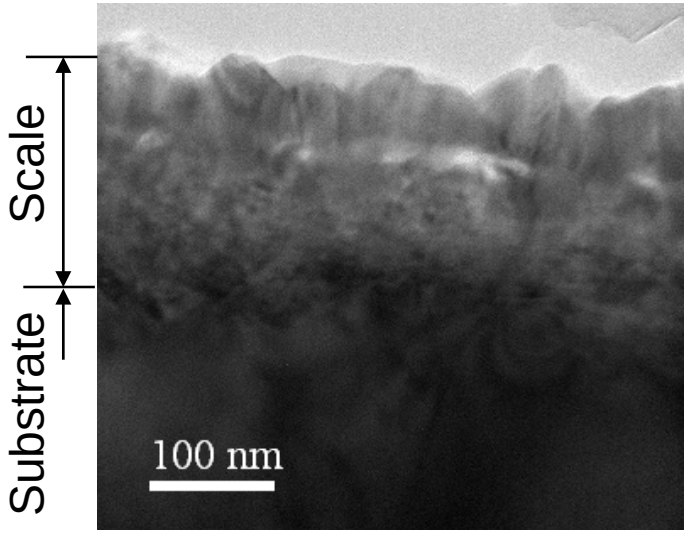
Scale
Substrate
100 nm

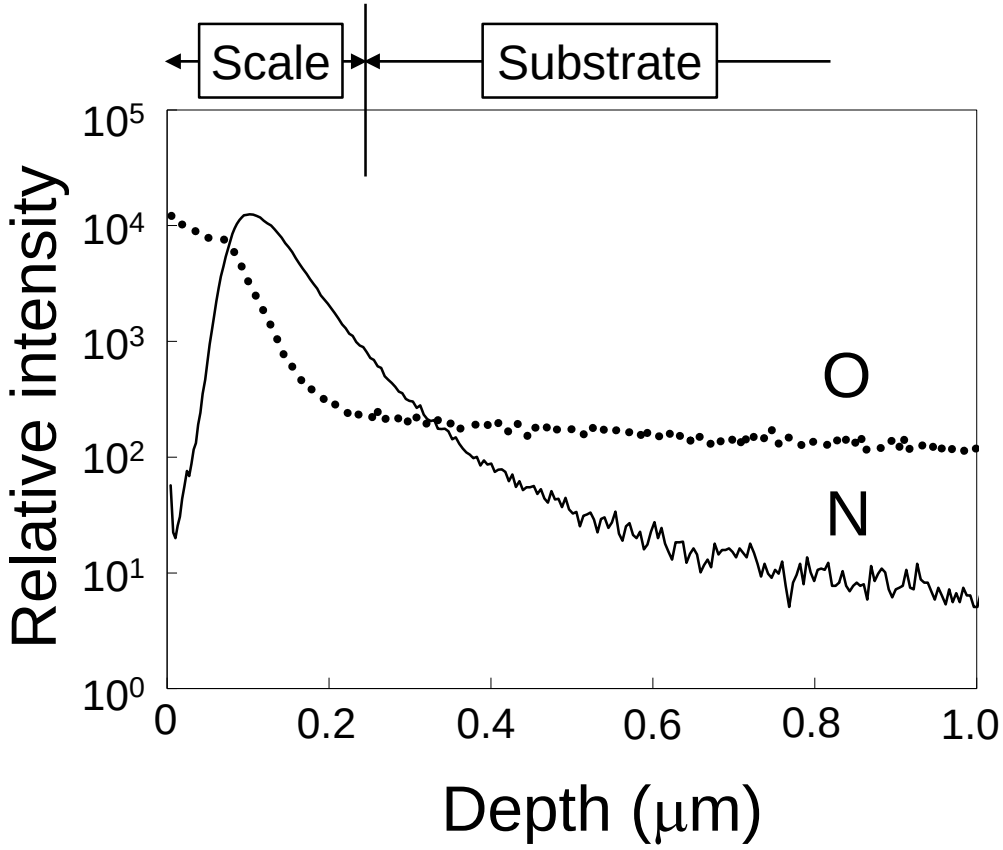
Scale
Substrate
Relative intensity
10^5
10^4
10^3
10^2
10^1
10^0
O
N
0
0.2
0.4
0.6
0.8
1.0
Depth (μm)

FIG. 1

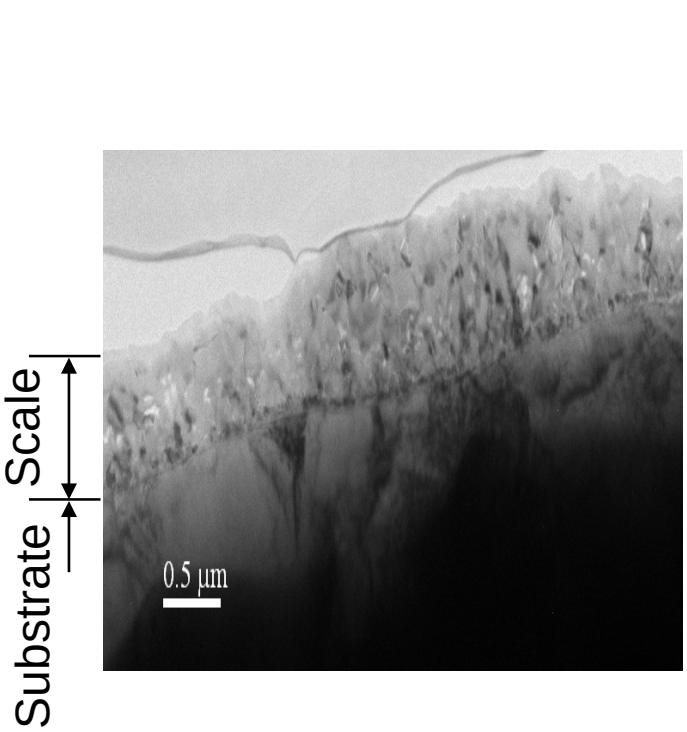
Scale
Substrate
0.5 μm

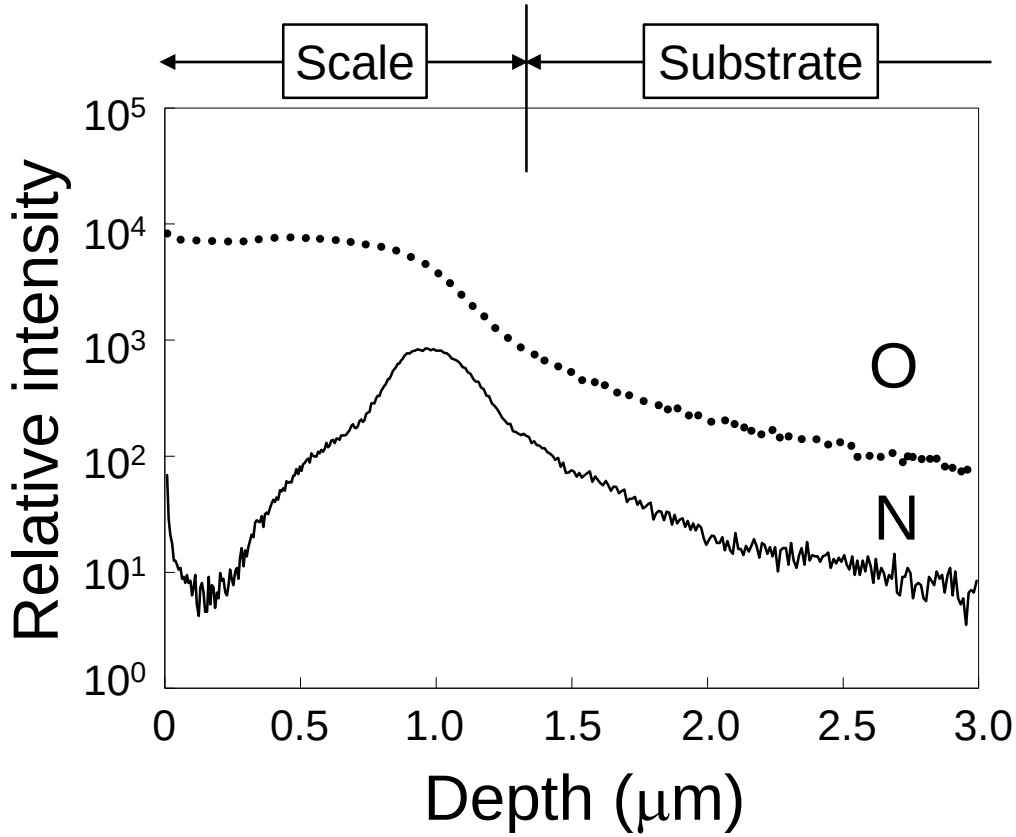
Scale
Substrate
Relative intensity
10^5
10^4
10^3
10^2
10^1
10^0
O
N
0
0.5
1.0
1.5
2.0
2.5
3.0
Depth (μm)

FIG. 2

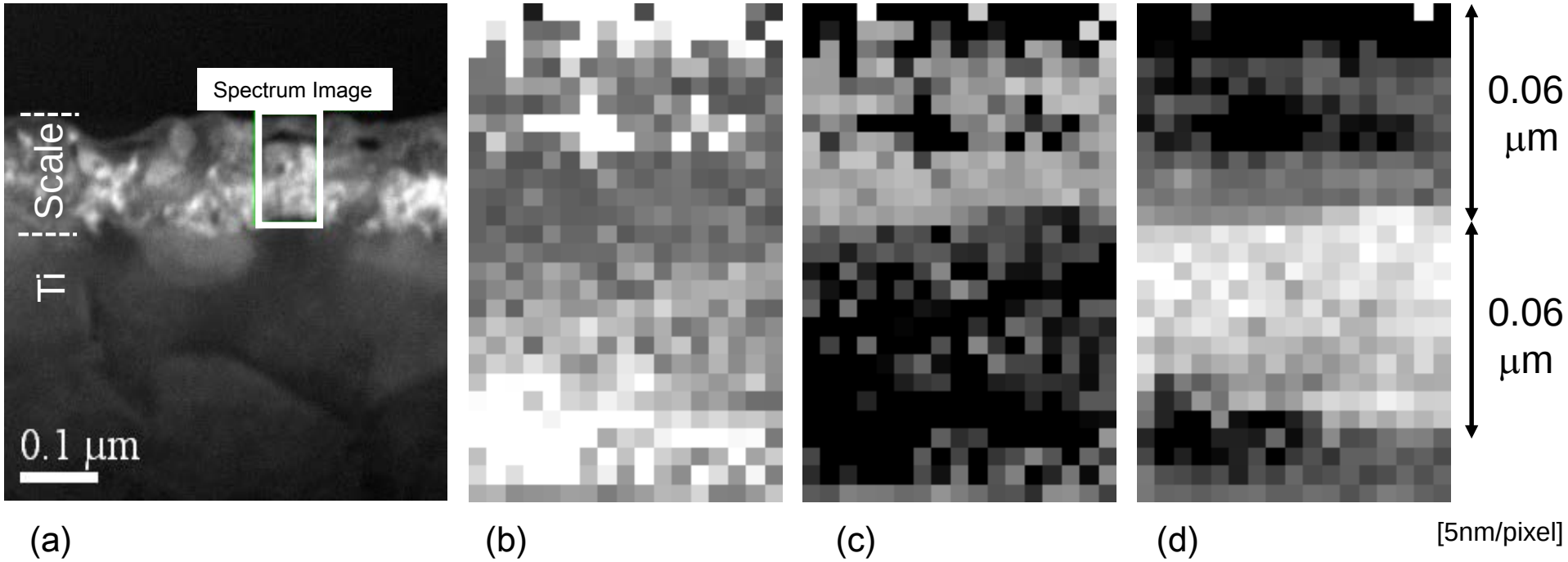
Ti distribution
O distribution
N distribution
Spectrum Image
Scale
Ti
0.1 μm
0.06 μm
0.06 μm
(a)
(b)
(c)
(d)
[5nm/pixel]

FIG. 3

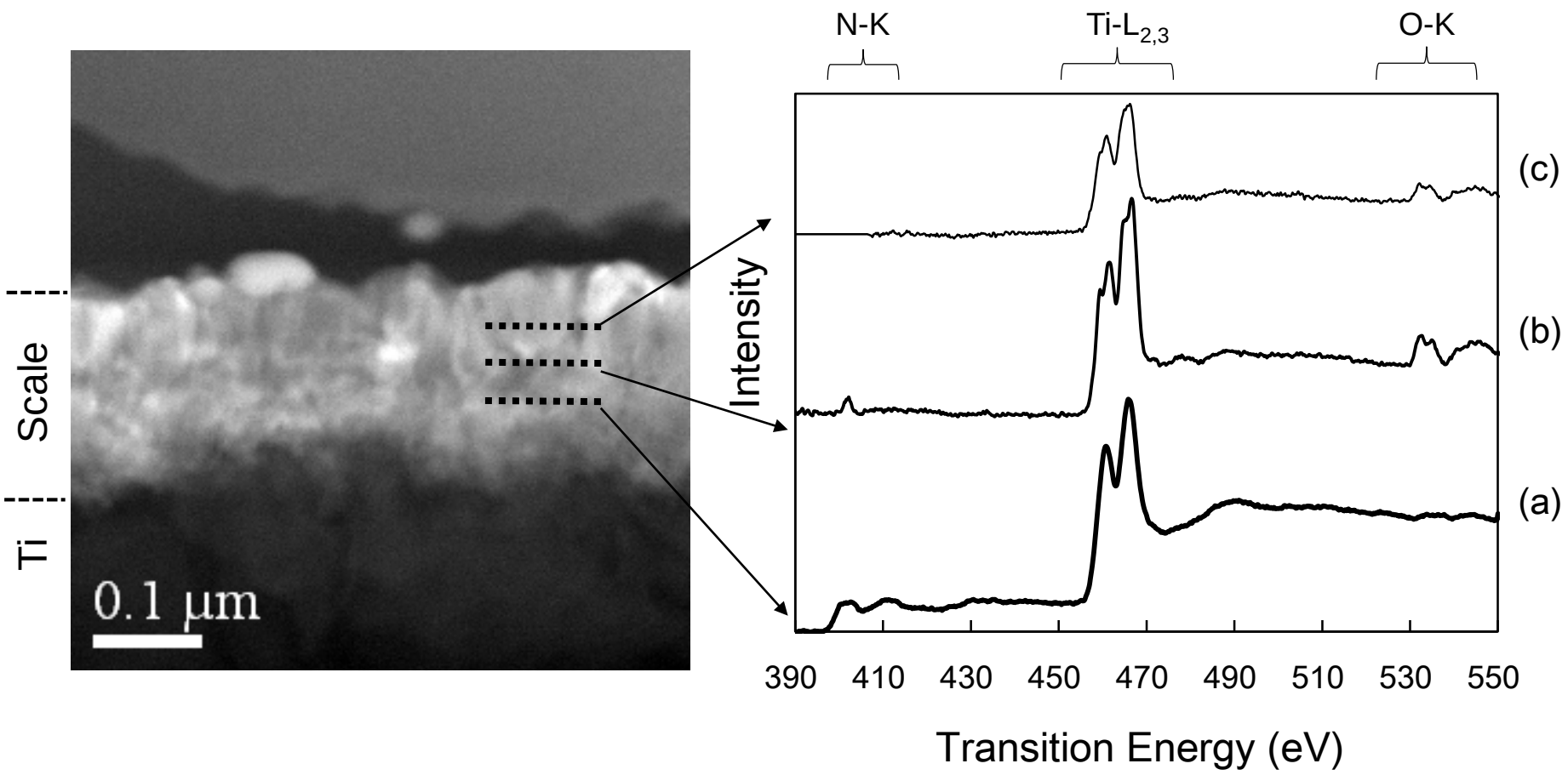
Scale
Ti
0.1 μm
N-K
Ti-L2,3
O-K
Intensity
(c)
(b)
(a)
390
410
430
450
470
490
510
530
550
Transition Energy (eV)

FIG. 4

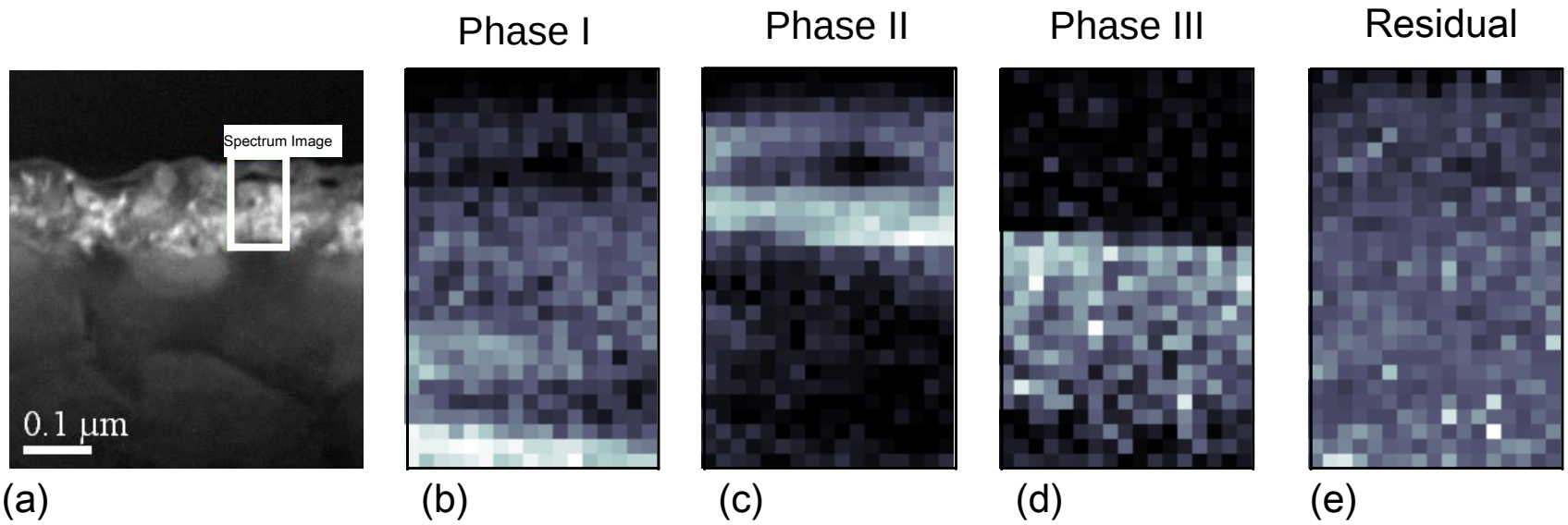
Phase I
Phase II
Phase III
Residual
Spectrum Image
0.1 µm
(a)
(b)
(c)
(d)
(e)

FIG. 5

	Phase	Type
.....	I	Ti
———	II	N-doped TiO_2
- - - - - - - -	III	TiN

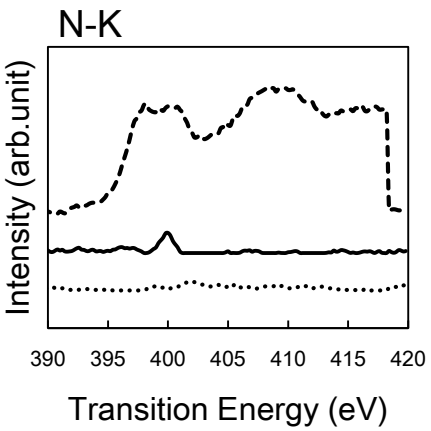

(a)

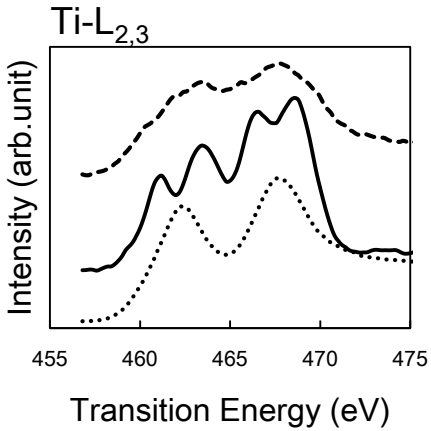

(b)

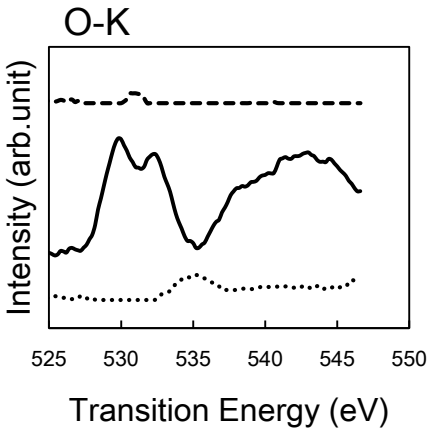

(c)

FIG. 6

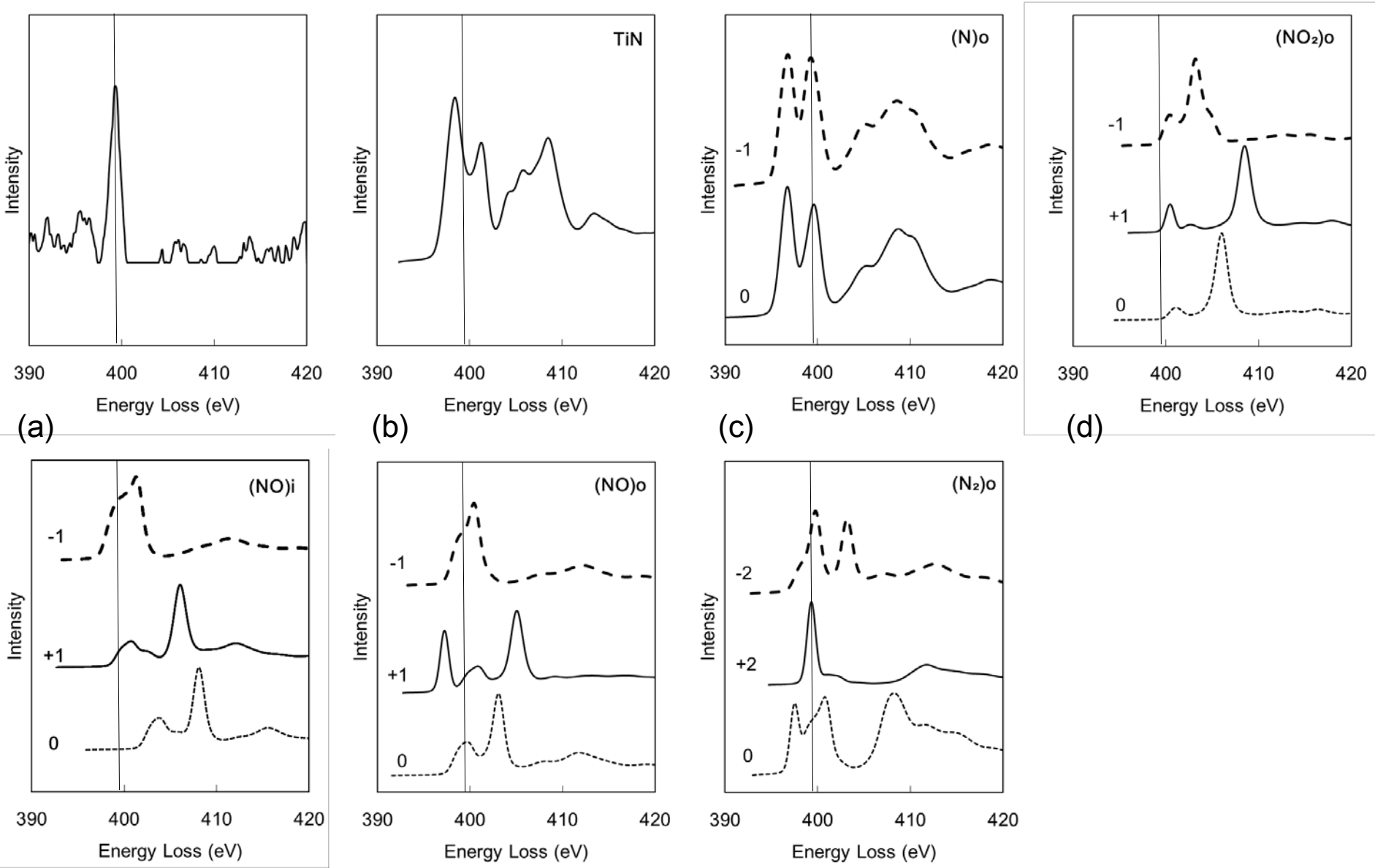
Intensity
390
400
410
420
Energy Loss (eV)
(a)
TiN
(b)
(N)o
-1
0
(c)
(NO₂)o
-1
+1
0
(d)
(NO)i
-1
+1
0
(e)
(NO)o
-1
+1
0
(f)
(N₂)o
-2
+2
0
(g)

FIG. 7

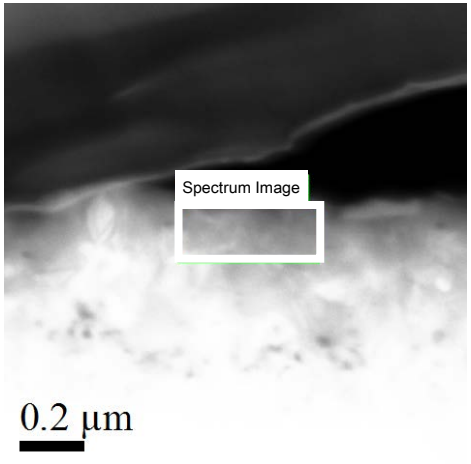

(a)

Phase I

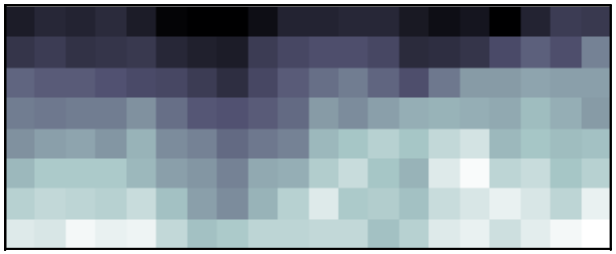

(b)

Phase II

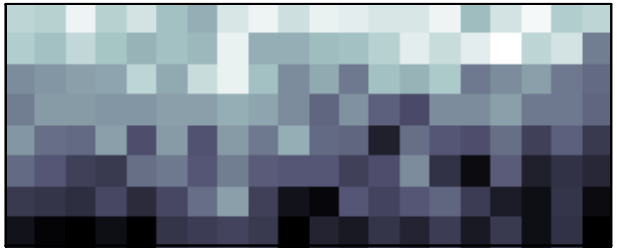

(c)

Residual

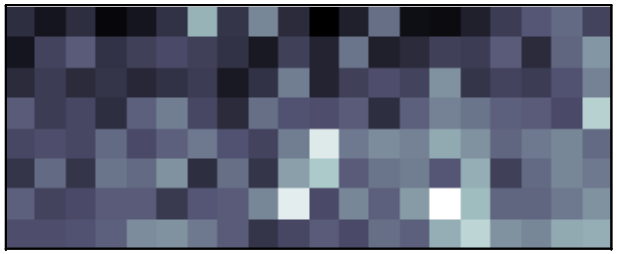

(d)

FIG. 8

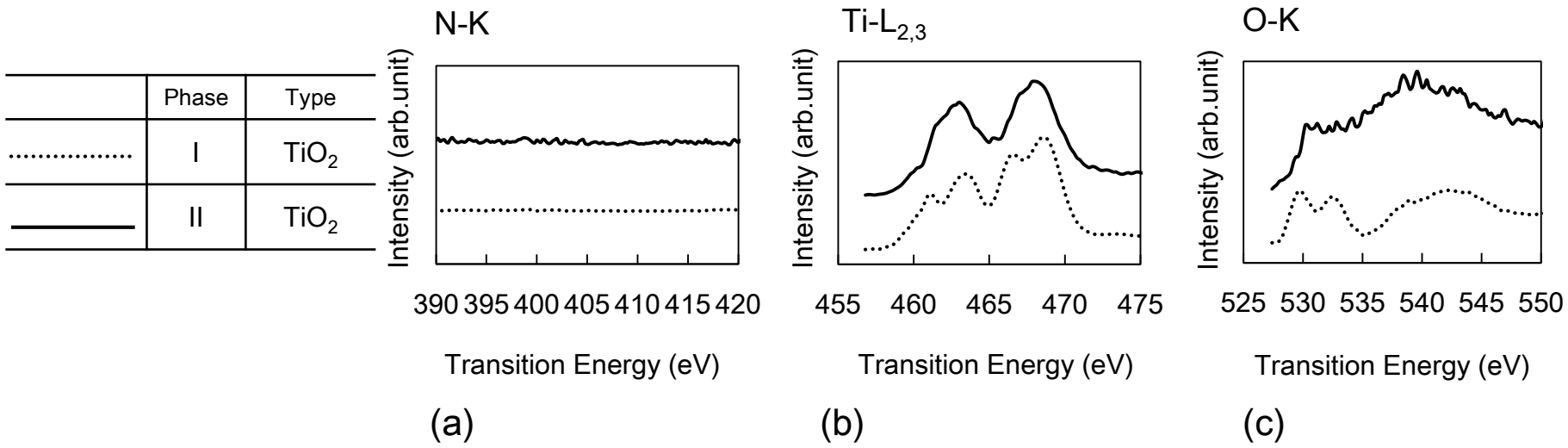
Phase
Type
I
TiO_2
II
TiO_2
N-K
Intensity (arb.unit)
390 395 400 405 410 415 420
Transition Energy (eV)
(a)
Ti-$L_{2,3}$
Intensity (arb.unit)
455 460 465 470 475
Transition Energy (eV)
(b)
O-K
Intensity (arb.unit)
525 530 535 540 545 550
Transition Energy (eV)
(c)

FIG. 9